Getting ViT in Shape:
Scaling Laws for Compute-Optimal Model Design

Ibrahim Alabdulmohsin⋆, Xiaohua Zhai⋆, Alexander Kolesnikov, Lucas Beyer⋆
Google DeepMind
Zürich, Switzerland
{ibomohsin,xzhai,akolesnikov,lbeyer}@google.com

Abstract

Scaling laws have been recently employed to derive compute-optimal model size (number of parameters) for a given compute duration. We advance and refine such methods to infer compute-optimal *model shapes*, such as width and depth, and successfully implement this in vision transformers. Our shape-optimized vision transformer, SoViT, achieves results competitive with models that exceed twice its size, despite being pre-trained with an equivalent amount of compute. For example, SoViT-400m/14 achieves 90.3% fine-tuning accuracy on ILSRCV2012, surpassing the much larger ViT-g/14 and approaching ViT-G/14 under identical settings, with also less than half the inference cost. We conduct a thorough evaluation across multiple tasks, such as image classification, captioning, VQA and zero-shot transfer, demonstrating the effectiveness of our model across a broad range of domains and identifying limitations. Overall, our findings challenge the prevailing approach of blindly scaling up vision models and pave a path for a more informed scaling.

1   Introduction

The de-facto approach for improving performance of vision and language models today is scale: large models are trained on more data for longer [61, 40, 23, 18, 76, 22, 12, 15]. Empirically, it has been observed that the benefit of scale often follows a predictable power law in which the performance $f(x)$ (e.g. error rate or log-perplexity) satisfies $f(x) \sim \beta x^{-c} + \varepsilon_\infty$ for some $\beta, c > 0$ as one varies the scaling dimension x (e.g. data or model size), if the remaining dimensions are not bottlenecks [31, 36, 26, 25, 3, 1]. Here, ε_∞ is the irreducible loss.

However, the simple power-law relation becomes more complicated when compute is considered. In this case, power laws are observed *only* along the compute-optimal frontier. Otherwise, scaling up the model size for a fixed compute budget can deteriorate performance (see [36, 32] and Figure 4). Since one often has a fixed compute budget in mind (e.g. available hardware and time), one should pick the model size that maximizes performance subject to the compute budget constraint, which may imply not training until convergence. Indeed, this approach was used successfully in the recent Chinchilla [32] that outperformed its predecessor Gopher [52] despite being $4\times$ smaller in size.

Unfortunately, in both [36] and [32] among others, the "size" of a model is equated with its parameter count, with no special consideration for model "shape dimensions", such as "depth" or "width". The rationale behind this choice follows from the surprising observation that the transformer shape had little impact on its scaling behavior in language modeling (LM) when performance is measured upstream (e.g. using log-perplexity) [36, 29, 30]. Nevertheless, follow-up analysis suggests that shape plays a pivotal role in other domains, such as in machine translation [44] and also in language

---
⋆Significant technical contributions.

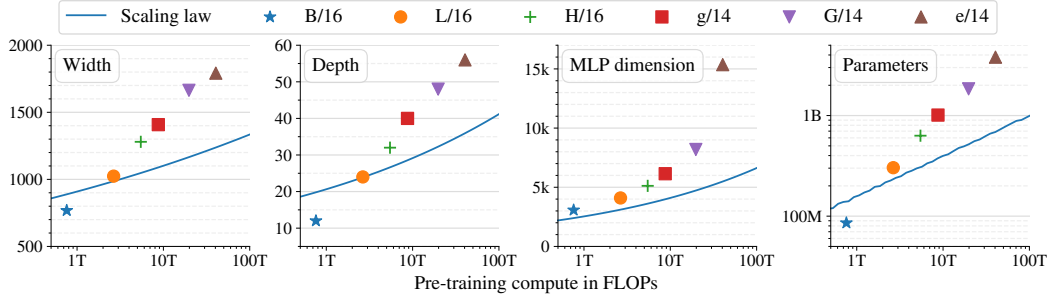arXiv:2305.13035v1 [cs.CV] 22 May 2023

Figure 1: Predicted efficiency frontier (depth, width, MLP dimension, and parameter count) in SoViT. In large models, optimal shapes follow a similar trajectory in both image classification and multimodal tasks (see Section 4) although they can be different in small models (see Figure 3).

modeling for *downstream* performance [63], with recent works even advocating for extreme aspect ratios, such as a single wide attention layer [11].

In vision, in particular, much earlier works using convolutional neural networks (CNNs) pointed out that the parameter count is indeed a poor predictor of performance. For example, scaling all dimensions [61, 40, 4] in ResNets [28] is more effective than scaling a single dimension such as depth alone. In addition, scaling width [75] is often more effective than depth, especially for small models [33, 55, 71]. Hence, optimizing the "shape" of transformers seems worthwhile.

In this work, we present **SoViT**: a **s**hape-**o**ptimized **vi**sion **t**ransformer [23] that matches the performance of much larger models despite being pre-trained with equal compute. It is derived from a recipe we introduce for optimizing the shape of neural architectures, such as their depth and width. A principled approach for scaling multiple dimensions is advantageous because although one can scale dimensions via brute-force search, this requires extensive computation and often remains sub-optimal [61]. Our recipe allows us to extrapolate without having to conduct an extensive set of experiments. For example, after only 115 experiments, we identify a scaling strategy in ViT for *all* three dimensions: width (internal representation), depth, and MLP size. For comparison, [32] requires over 400 experiments to optimize a single dimension (the parameter count) alone.

One major finding is that small vision models can perform on par with larger ones with the *same compute* if we optimize their shape. In language, recent works have demonstrated the value of scaled-down architectures, such as the Chinchilla model [32] discussed earlier — a 70B parameter model that outperforms the 280B-parameter Gopher [52] and 175B-parameter GPT3 [12] — as well as LLaMA with its 13B parameter variant outperforming GPT3 on most benchmarks [66]. By introducing SoViT, we establish this phenomenon in vision as well.

Figure 1 summarizes how the various shape dimensions are scaled in SoViT (see Section 3 for derivation). The MLP dimension is scaled faster than depth, which in turn is scaled faster than width. When summarized by their parameter count (rightmost plot), compute-optimal ViTs are smaller than was previously used. With this scaling strategy, we find the shape of a ViT for the compute-equivalent of ViT-g/14 [76] pretrained on 16B JFT images [60]. We call this 2.5× smaller model SoViT-400m/14. It achieves 90.3% fine-tuning accuracy on ILSRCV2012 [21] and 82.2% zero-shot accuracy in the locked-image text tuning (LiT) setup [77]. We further evaluate SoViT-400m/14 on captioning, VQA and panoptic segmentation and highlight some results in Figure 2.

Statement of Contribution. In summary, our contribution is to:

- Introduce a new method for optimizing *the shape* of neural networks, such as their depth and width. Our technique expands and improves previous methods by optimizing *multiple* shape dimensions *jointly* while requiring significantly fewer experiments.

- Demonstrate the effectiveness of scaled-down architectures in vision. We optimize ViT for the compute-equivalent of ViT-g/14, leading to a smaller, faster model of equal quality.

- Present new qualitative insights for scaling vision transformations, such as on how to scale individual shape dimensions and how optimal ViT shapes vary across domains.
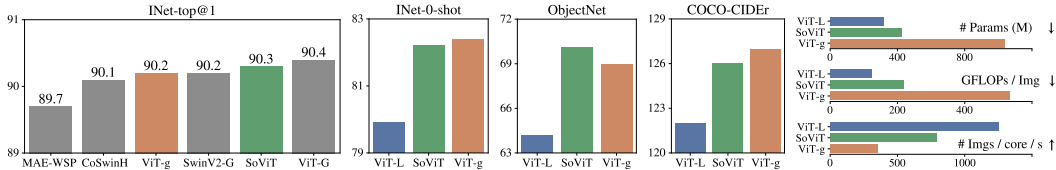
2

Figure 2: Optimizing for the compute-equivalent of ViT-g/14 results in the $2.5\times$ smaller SoViT-400m/14 model achieves equivalent results across a wide range of benchmarks. Our model performs exceptionally well on the competitive ImageNet (ILSRCV2012) benchmark in comparison with significantly larger models from the recent literature [58, 74, 46, 76].

- Conduct extensive evaluation across tasks like image classification, image captioning, VQA, zero-shot classification and panoptic segmentation, identifying both gains and limitations.

2 Related Work

Optimizing training for compute has received a significant amount of attention in recent years, partly due to the financial and environmental costs of training large models [49, 52]. However, conflicting results are sometimes reported. For example, in language modeling, [36] argues that the model size should be scaled faster than the data size, implying it is compute optimal to "undertrain" large models. Similar conclusions are found in [44]. On the other hand, [32] argues that the model size should be scaled uniformly with the data size, and highlights that transformers were not trained long enough, leading to some recent efforts [66] "overtraining" their models instead. Our analysis for ViT in Section 4 agrees partially with the latter result.

Scaling the size of vision transformers has led to remarkable results achieving, for instance, 90.4% top-1 accuracy on ImageNet (ILSRCV2012) with 2 billion parameters [76] and 90.9% top-1 accuracy with 4 billion parameters [14]. When scaled to 22 billion parameters, ViT exhibits state-of-the-art alignment to human visual perception in terms of shape/texture bias, among other findings [20].

Despite the clear benefit of scale, there has been little investigation into optimally scaling the shape of ViTs. [63] suggest preferentially increasing depth before scaling other dimensions uniformly. For ViT, however, they only consider small ViT-S and ViT-B models and the reported accuracy improvement comes with an *increase* in FLOPs of up to $\times 4$, making it difficult to draw conclusions about the suggested shape's quality. In contrast [11] recommend scaling width over depth, but the authors do not observe any improvement when applying their strategy to ViT.

Our analysis draws inspiration from "compound scaling" in MobileNet [33] and EfficientNet [61], while differing in significant ways. EfficientNet uses an exhaustive grid search to determine the optimal architecture for a fixed increase in compute (e.g. $\times 2$). Afterwards, each dimension is scaled up by the same ratio with every subsequent increase in compute. In contrast, we expand scaling laws to simultaneously account for model size and compute beyond the efficient frontier and leverage them to derive the optimal scaling exponents for each dimension separately, as outlined in Section 3.

Throughout our analysis, we use *downstream* metrics, e.g. ImageNet 10-shot error, when measuring performance instead of upstream metrics. This follows recent reports arguing that upstream performance may not reflect downstream performance in language and vision [62, 76].

We use GFLOPs as a proxy for compute since it is hardware-agnostic and correlates well with actual wall-clock core-hours (see Figure 4). However, GFLOPs can have limitations [4, 19] and may not be a perfect predictor for the metric of interest (e.g. core hours) in all model and hardware types. Note that we focus on scaling the shape of the architecture, not on improving its training protocol, which can be similarly beneficial [4, 64, 59, 65].

3 Scaling Strategy

Notation. We begin with a formal description of the problem. We represent a neural architecture as a tuple $\mathbf{x} = (\mathbf{x}_1, \mathbf{x}_2, \ldots, \mathbf{x}_D) \in \mathbb{N}^D$ containing D shape dimensions, such as width, depth and MLP
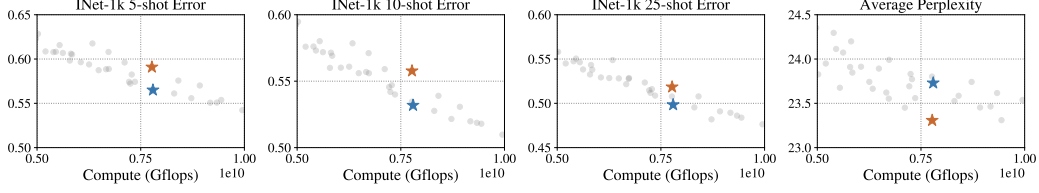
Figure 3: A grid sweep over multiple ViT shapes pretrained on 600M JFT examples highlights the important role of shape. The two architectures marked in blue and red are compute-optimal for image classification and image-to-text tasks (captioning/VQA), respectively. For captioning/VQA, we average log-perplexity scores (see Section 4.2). In *small* models, an optimal shape in one domain is not necessarily optimal in others.

size. We denote compute such as GFLOPs by $\mathbf{t}$. We designate $f : \mathbb{N}^D \times \mathbb{R}^+ \to \mathbb{R}$ a performance metric of interest, such as downstream ImageNet 10-shot error rate. Specifically, $f(\mathbf{x}, \mathbf{t})$ results from (pre)-training an architecture $\mathbf{x}$ for a fixed compute budget $\mathbf{t}$. We always assume that f corresponds to a loss, meaning lower values are better.

The goal of optimizing shape for fixed compute $\mathbf{t}$ is to identify $\mathbf{x}^\star$ (depending on $\mathbf{t}$) such that:

$$f(\mathbf{x}^\star, \mathbf{t}) - \inf_{x \in \mathbb{N}^D} f(x, \mathbf{t}) \ \leq \ \epsilon, \tag{1}$$

for some small tolerance $\epsilon > 0$. Due to modeling assumptions, approximations, and the finite possible number of experiments conducted, we cannot hope for $\epsilon = 0$ and have to tolerate a small excess loss.

Single Dimension. As demonstrated in Figure 3, the shape of a pretrained vision transformer has an impact on its downstream performance. To determine an optimal shape scaling strategy, we begin by considering both compute $\mathbf{t}$ and a *single* shape dimension $\mathbf{x}_k$ for $k \in [D]$, such as depth. In prior works, optimizing a single dimension $\mathbf{x}_k$ for compute involves running a large number of experiments in order to identify the Pareto optimal frontier, from which power laws on $\mathbf{x}_k$ or $\mathbf{t}$ are derived [36, 32]. Since this is expensive, we propose the following joint functional form instead:

$$f_k(\mathbf{x}_k, \mathbf{t}) \sim \alpha_k \mathbf{x}_k^{-a_k} + (\beta_k \mathbf{x}_k^{b_k} + \xi_k)\,\mathbf{t}^{-c} + \varepsilon_k, \tag{2}$$

where $\alpha_k, a_k \beta_k, b_k, c, \xi_k, \varepsilon_k > 0$. Here, f_k focuses on the dimension k alone and assumes that all other shape dimensions $j \neq k$ are sufficiently large such that they do not constitute a bottleneck. We also assume that data is unlimited so that there is no risk of overfitting. Our argument for this particular functional form is six-fold:

I. If compute is unbounded, we recover the familiar power law relation on model size $f_k(\mathbf{x}_k) \sim \alpha_k \mathbf{x}_k^{-a_k} + \varepsilon_k$ [31, 2, 35, 36].

II. For any *fixed* model size, the relation above reduces to the power law $f_k(\mathbf{t}) \sim A\mathbf{t}^{-c} + B$, where $A = \beta_k \mathbf{x}_k^{b_k} + \xi_k$ and $B = \alpha_k \mathbf{x}_k^{-a_k} + \varepsilon_k$. Since the model size is fixed, $\mathbf{t}$ is proportional to the size of the data. Such data scaling laws have been demonstrated extensively in various domains [1–3, 26, 31, 36, 56, 76].

III. For fixed compute, the relation w.r.t. $\mathbf{x}_k$ is non-monotone, quasiconvex (see Appendix A), in agreement with empirical measurements [36, 32]. See IsoFlop curves in Figure 4.

IV. Arguments for power law behavior using space partitioning suggest that the exponent c is independent of the shape dimension. In particular, $c = \Theta(1/d)$, where d is the intrinsic dimension of the data manifold [2, 35, 56]. From this, we conclude that assuming the functional form in (2) for every shape dimension *separately* cannot lead to any contradictions since this assumption is satisfied by the decomposable loss:

$$f(\mathbf{x}, \mathbf{t}) = \sum_k \alpha_k \mathbf{x}_k^{-a_k} + \sum_k \beta_k \mathbf{x}_k^{b_k} \mathbf{t}^{-c} + \xi \mathbf{t}^{-c} + \varepsilon_\infty, \tag{3}$$

for some constants $\xi, \varepsilon_\infty > 0$.

V. When optimizing the shape dimension $\mathbf{x}_k$ for fixed compute $\mathbf{t}$, the optimal value $\mathbf{x}_k^\star$ is:

$$\mathbf{x}_k^\star = \left(\frac{\alpha_k\, a_k\, \mathbf{t}^c}{\beta_k b_k}\right)^{\frac{1}{b_k + a_k}} = O\left(\mathbf{t}^{s_k}\right), \quad \text{where: } s_k = \frac{c}{b_k + a_k}. \tag{4}$$

4

Recall that the scaling exponent s_k in (4) is positive because $a_k, b_k, c > 0$. Using the relation (4), we rearrange the terms in Eq. (2), and obtain the scaling law for model performance along the compute-optimal frontier (Appendix A):

$$f_k(\mathbf{x}_k, t) = F\mathbf{x}_k^{-a_k} + G\mathbf{t}^{-c} + \varepsilon_k, \qquad \text{(in the compute-optimal frontier)} \qquad (5)$$

for some constants F and G, which is a sum of power law terms involving the model size and compute. Indeed, this decomposition has been demonstrated to hold within the compute-optimal frontier by [36] and [32].

VI. Eq. (2) fits empirical measurements and extrapolates accurately as well, see Figure 4.

Multiple Dimensions. Next, we expand upon the previous approach by incorporating multiple dimensions. To reiterate, our method involves both a functional form (2) and a novel procedure. Our procedure significantly decreases the number of large-scale experiments required to identify compute-optimal architectures, by an order of magnitude compared to prior work [32].

Star Sweep – Conducting a brute-force grid search to estimate scaling parameters across all dimensions is expensive, since it requires $O(2^D)$ experiments to cover the search space. Instead, we demonstrate that a "star sweep" is sufficient: (1) starting from a *large* model $\mathbf{x}^{(c)}$ (the star center), we vary a single dimension $k \in [D]$ at a time in an exponentially-spaced grid, such that all values are much smaller than $\mathbf{x}_k^{(c)}$. In our experiments, for instance, we optimize three shape parameters: `width`, `depth`, and `MLP dim`. Our star center is $\mathbf{x}^{(c)} = (1968, 40, 6144)$; i.e. has `width` 1968, `depth` 40, and `MLP dim` 6144. When varying `MLP dim` in the star sweep, we use the grid $(1088, 1360, 1728, 2160, 2592, 3072)$, corresponding to about 20% increase in each step, while fixing `width` to 1968 and `depth` to 40. We do this to ensure that other dimensions do not form a bottleneck when estimating the parameters in (2). This gives us the scaling exponents s_k in (4).

Grid Sweep – The second stage is a grid sweep for *small* models trained for *short* compute. The cost of running this grid sweep is negligible. Its goal is to identify a single architecture $\mathbf{x}^{(0)}$ that lies in the Pareto optimal frontier for small compute as illustrated in Figure 3. This is important since a suboptimal $\mathbf{x}^{(0)}$ can significantly skew results [4]. Our grid sweep identifies $\mathbf{x}^{(0)}$ to be $(608, 10, 928)$, the blue star in Figure 3. The advantage of this step is to absorb the leading coefficients in $\mathbf{x}_k^\star = O(\mathbf{t}^{s_k})$ in (4) so that the star sweep focuses on estimating the *exponents* s_k alone. We demonstrate in Figure 5 that the scaling exponents s_k are robust to the choice of the evaluation metric f.

Scaling. Finally, we scale all dimensions jointly. Starting from the small compute-optimal architecture $\mathbf{x}^{(0)}$ and the amount of compute $\mathbf{t}^{(0)}$ it is optimal for, suppose we increase compute by a factor $\tau > 1$ (i.e. the new compute is $\tau \mathbf{t}^{(0)}$). By treating this increment τ as a *sequence* of D smaller increments of size $\tau^{1/D}$ each, an increase in compute by a factor of τ is accompanied by an increase in every shape dimension k by a factor of $\tau^{s_k/D}$, respectively.
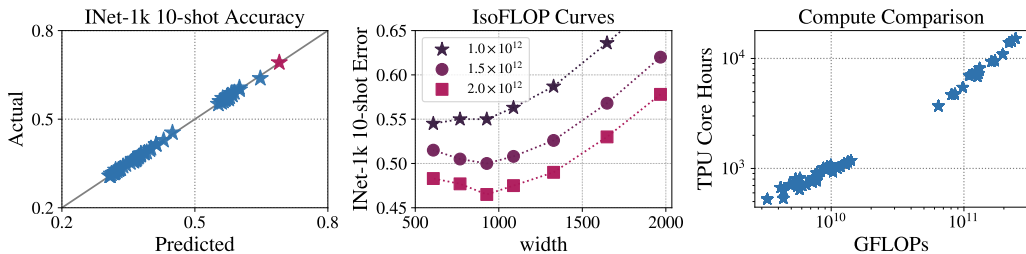

Figure 4: LEFT: Comparison between ILSRCV2012 (denoted INet-1k) 10-shot error rate predicted by Eq. (2) and actual. The value marked in **violet** corresponds to the star center $\mathbf{x}^{(c)}$ that is never used when estimating scaling parameters. Eq. (2) is consistent with empirical measurements and extrapolates accurately. MIDDLE: IsoFlop curves in ViT as one varies the width dimension. RIGHT: GFLOPs is well-correlated with actual TPU core hours across models (correlation coefficient ~ 0.99).
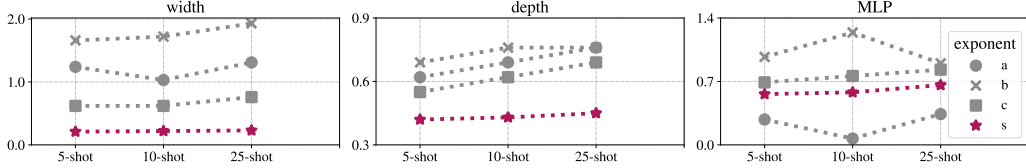
Figure 5: A plot of the estimated values of the exponents in (2) for different evaluation metrics f. The scaling exponent s_k tends to be less sensitive to the choice of metric than other exponents. Moreover, the data scaling exponent c is approximately $c \approx 0.65 \pm .06$, independently of the choice of the shape dimension, in agreement with what would be expected using space partitioning arguments [2, 35, 56].

4 Shape-optimized ViT

We implement the scaling strategy in Section 3 in vision transformers [23] pretrained on JFT-3B, a proprietary dataset with about 30k classes and around 3 billion examples [76], using the Adam optimizer [38]. As mentioned in Section 3, we focus on optimizing three shape dimensions: `width` (size of internal representation), `depth` and `MLP dim` (hidden dimension). Following [40, 23, 76], we remove near-duplicate examples between upstream JFT-3B data and all the downstream train and test sets. Appendix B contains the full set of hyper-parameters used in the experiments, including full details about the star and grid sweeps described in Section 3. We fix the patch size in our analysis to 14×14, but study "flexifying" to arbitrary sequence lengths following [6] in Section 5.5.

As an evaluation metric f, we consider two domains: (1) image classification, with ImageNet linear 10-shot error rate as the metric, and (2) image-to-text LiT-decoding following [7]. In the latter case, the evaluation metric f is an average of four perplexity scores: COCO captioning, optical character recognition (OCR), and question answering (VQAv2 and GQA). Refer to [7] for details about the LiT-decoder setup. By considering such distinct domains, our goal is to identify similarities and differences (if any) in how to optimally scale the shape of vision transformers (ViT).

4.1 Image Classification

We use the aforementioned star center $\mathbf{x}^{(c)} = (1968, 40, 6144)$ as our starting point. To estimate the scaling exponents s_k in (4) for each dimension separately, we vary `width` in the grid (608, 768, 928, 1088, 1328, 1648), `depth` in the grid (8, 10, 12, 16, 20, 24), and `MLP dim` in the grid (1088, 1360, 1728, 2160, 2592, 3072). As discussed in Section 3, we use an exponential spacing with all values being much smaller than in the star center $\mathbf{x}^{(c)}$. Following [23], we evaluate quality using few-shot linear transfer by using pre-trained models to extract features and fitting a linear regression head mapping them to the one-hot encoding of the target labels.

The individual scaling exponents we find are $s_{\text{depth}} \approx 0.45$, $s_{\text{width}} \approx 0.22$, and $s_{\text{MLP}} \approx 0.6$. Importantly, these exponents are quite robust to the choice of the metric. As shown in Figure 5, changing the metric from ImageNet 10-shot to either 5-shot or 25-shot can change the best-fit estimate of the other exponents a_k, b_k, c_k in (2) but the scaling exponent s_k is relatively unchanged, since it is formed as a *ratio* over other exponents. In addition, the data scaling exponent c appears to be independent of the choice of the shape dimension. As mentioned earlier, this is consistent with space partitioning arguments for power law scaling [2, 35, 56].

The estimated scaling exponents s_k point to the following picture:

I. MLP dimension should be scaled faster than depth, and depth faster than width. An easy-to-remember rule of thumb could be: $\text{MLP} \approx \Theta(\text{Depth}^{1.5})$ and $\text{Depth} \approx \Theta(\text{Width}^{1.5})$.

II. The size of ViT, as quantified by its parameter count, is scaled more slowly than the allocated compute. More precisely, for every increment in compute by a factor of 10, the parameter count of the optimized model shape increases by a factor of ≈ 7.

III. As demonstrated in Figure 1, small ViT models can match the performance of much larger ones when their shape and training duration are jointly optimized for the available compute.

We validate these predictions by optimizing the shape of ViT for the compute-equivalent of ViT-g/14 when the latter is pretrained on 16 billion JFT-3B examples as done in [76]. The resulting model,
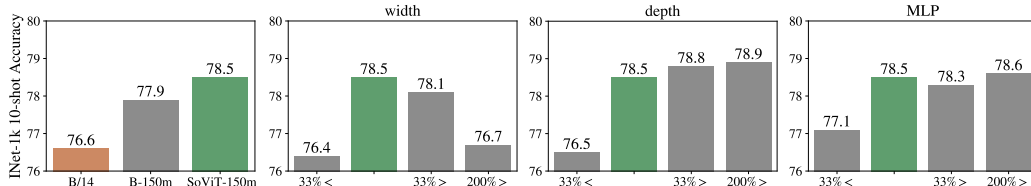
6

Figure 6: LEFT: Optimizing ViT shape for the compute-equivalent of ViT-B/14 results in SoViT-150m/14, which improves performance significantly. See Section 4.1. CENTER & RIGHT: Impact of debiating from the optimal shape in SoViT-150m/14 (in green) while keeping compute fixed.

SoViT-400m/14, is significantly smaller and faster, yet equally competitive. It has a `width` of 1152, `depth` 27, and `MLP dim` 4304. Fine-tuning it on ImageNet results in a 90.3% top-1 accuracy, see Figure 2. Section 5 presents various other evaluations.

In Figure 6, we also optimize the shape of ViT for the compute-equivalent of ViT-B/14 pretrained on 4 billion examples of JFT-3B using Imagenet 10-shot error rate as an evaluation metric, resulting in SoViT-150m/14. As shown in Figure 6, optimizing the shape of ViT leads to a significant improvement in performance, from 76.6% in ViT-B/14 to 78.5% in SoViT-150m/14 when both are trained for the same amount of compute. We also vary the optimized shape by decreasing/increasing one dimension at a time and retraining the corresponding model while keeping the total compute fixed. As shown in Figure 6, small deviations from the predicted optimal shape can lead to a notable drop in performance, especially for width since it has the smallest scaling exponent (see Figure 5). We also include in Figure 6 (LEFT) a comparison with a model, denoted B-150m, which has the same *shape* as ViT-B/14 but the same *size* as SoViT-150m/14. This confirms that while optimizing the model size improves performance, optimizing the shape improves it even further.

Importantly, the model shapes in Figure 6 bear no resemblance to those observed during the star or grid sweeps. To recall, the star sweep is centered around an architecture $\mathbf{x}^{(c)}$ whose shape dimensions are significantly larger than in ViT-B/14, whereas the grid sweep pretrains models that are substantially smaller and for only 600M examples. The ability of our strategy to accurately identify a near-optimal model shape within this context underscores its robust extrapolation capability.

4.2 Multitask Decoder

Besides image classification, there has been a significant interest in multimodal applications, mostly fueled by the convergence across language and vision on the transformer architecture [69, 23]. In particular, an encoder-decoder transformer with an autoregressive decoder is a popular choice because it allows reusing pretrained image encoders. We repeat the analysis conducted in Section 4.1 to optimize the shape of the image encoder, while fixing the decoder architecture to two layers as was used in [7]. Further details are provided in Appendix C. As an evaluation metric f, we use the average of four perplexity scores: COCO captioning [45, 13], OCR [47], VQAv2 [27] and GQA [34], without normalization since they share a similar scale. For the learning rate and weight decay hyper-parameters, we conduct a sweep where we vary the learning rate in $\{10^{-3}, 3 \times 10^{-4}, 10^{-4}\}$ and the weight decay in $\{3 \times 10^{-4}, 10^{-4}, 3 \times 10^{-5}\}$. We pick the largest learning rate and the corresponding weight decay that result in a stable training run (i.e. smooth training loss curve and gradient norms) for both the largest and smallest image encoder architectures. From this, a learning rate of 3×10^{-4} and a weight decay of 10^{-4} are selected.

Using this analysis, the derived scaling exponents are approximately $0.25, 0.49$ and 0.62 for `width`, `depth` and `MLP size`, respectively. Hence, whereas the optimal shape dimensions in small architectures can be quite different between image classification and multitask decoding, as shown in Figure 3, the scaling exponents are nearly identical, so the same scaling recipe is used in both domains.

5 Evaluations

Overview. We now evaluate SoViT-400M in various contexts to verify whether it broadly matches ViT-g/14's performance, or only in the ILSRCV2012 10-shot metric it was optimized for. The

settings we cover are few-shot, frozen linear probes on ImageNet, zero-shot transfer, image-language multitasking including captioning, OCR, and question answering, as well as panoptic segmentation. In each of these settings, we compare SoViT-400m/14 to ViT-L/16 and a ViT-g/14, all trained on the JFT-3B dataset as in [76].

Compute. Experiments are executed on Tensor Processing Units (TPU). SoViT-400m/14 is pre-trained on 40 billion examples, which amounts to 9T GFLOPs and 155K TPUv3 core-hours. ViT-g/14 was pretrained on 16 billion examples, corresponding to 9T GFLOPs and 210K TPUv3 core-hours. Thus, while GFLOPs are matched, ViT-g/14 was trained for 35% longer in terms of wall-clock time.

5.1 Image Classification

We verify classification performance in three common and widely useful setups: full fine-tuning, linear probes on the frozen model, and few-shot linear classification.

Table 1: ImageNet fine-tuning. The top shows models trained in the same controlled setting, and the bottom a representative set of large well-performing models. SoViT compares favorably. Contrary to common practice, we use a held-out 2% of Train to select hyper-parameters. Selecting them on Val would increase all scores. FLOPs according to XLA; PyTorch reports MACs.

Model	Pretraining	Size			ImageNet variant		
		Input	Params	FLOPs	Val [54]	ReaL [5]	v2 [53]
SoViT-400m/14	JFT-3B	224^2	428 M	221 G	88.9	90.3	80.7
ViT-L/16 [76]	JFT-3B	384^2	303 M	383 G	88.5	90.4	80.4
SoViT-400m/14	JFT-3B	384^2	428 M	672 G	90.0	90.9	83.2
ViT-g/14 [76]	JFT-3B	518^2	1011 M	3208 G	90.2	90.9	-
SoViT-400m/14	JFT-3B	518^2	428 M	1374 G	90.3	91.0	83.4
ViT-G/14 [76]	JFT-3B	518^2	1882 M	5668 G	90.4	90.8	83.3
SwinV2-G [46]	IN-21k + 70M	640^2	3000 M	?	90.2	-	84.0
CoAtNet-6 [18]	JFT-3B	512^2	1470 M	1521 G	90.4	-	-
MAE→WSP [58]	IG-3B	518^2	1890 M	5679 G	89.7	90.9	83.0
CoCa [73]	JFT-3B + ALIGN-1.8B	576^2	2100 M	?	91.0	-	-

Fine-tuning on ImageNet. Pre-trained image encoders are most commonly [17] evaluated by fine-tuning them on the ILSVRC2012 classification task. The detailed fine-tuning settings are provided in Appendix E. One important aspect is to increase image resolution [67] as a way of further increasing the capacity of the pre-trained model during fine-tuning [40]. Table 1 shows the performance of SoViT-400m/14 in comparison with ViT-L/16, ViT-g/14 fine-tuned at various resolutions, along with a few more representative models from the literature. The results confirm that SoViT-400m/14 achieves the goal of matching ViT-g/14 while being significantly smaller.

Linear probing on ImageNet. The quality of the pre-trained representation learned by the model is often more directly assessed by performing *linear probes*, meaning learning a linear classifier on top of unmodified, frozen output features from the model. We present results of this evaluation in Table 2, including robustness evaluations of the learned probe. SoViT-400m/14 is generally on par with ViT-g/14 despite its smaller output width.

Table 2: Linear ILSVRC2012 probes.

	Val	ReaL	v2	-R	-A	Obj
L/16	86.7	90.0	78.5	88.9	67.8	63.5
SoViT	88.2	**90.3**	80.6	89.0	76.4	**68.7**
g/14	**88.4**	90.2	**80.8**	**90.3**	**76.6**	67.7

Broad few-shot linear transfer. We follow [23, 76] and evaluate a closed-form linear regression probe for 10-shot classification across a wide range of tasks in Table 3.

Table 3: SoViT-400m/14 performs competitively with ViT-g/14 in 10-shot classification.

	INet [21]	CIFAR100 [43]	Pets [48]	Birds [70]	Caltech [24]	Cars [42]	Colorectal [37]	DTD [16]	UC [72]
ViT-L/16	81.5	82.2	97.0	97.1	89.9	93.8	79.4	72.0	96.3
SoViT-400m/14	**84.1**	86.7	**97.6**	**88.8**	**91.3**	93.6	**81.5**	72.5	97.7
ViT-g/14	84.0	**87.2**	97.4	88.5	89.3	**93.9**	78.9	**74.1**	**98.2**

Table 4: Summary of multitask decoding and zero-shot transfer results, see Sections 5.2 & 5.3.

Model	ImgNet	OCR-VQA [47]		GQA [34]		VQAv2 [27]		COCO Capt. [13]	
	Zero-shot	Acc [%]	Log-PPL	Acc [%]	Log-PPL	Acc [%]	Log-PPL	CIDEr	Log-PPL
ViT-L/16	79.9	48.3	17.9	55.3	24.9	66.4	20.9	120	28.7
SoViT-400M	82.2	**52.9**	**15.3**	56.0	23.9	67.7	20.9	**125**	**28.1**
ViT-g/14	**82.4**	52.5	15.9	**58.0**	**22.5**	**68.8**	21.5	126	27.9

5.2 Contrastive image-text tuning

Next, we follow the locked-image text tuning (LiT) recipe [77] on the WebLI dataset [14] to add zero-shot classification abilities to the pre-trained ViT-L/16, SoViT-400m/14 and ViT-g/14 image encoders. In this setup, a new text encoder is trained using the contrastive image-text matching objective [51]. See Appendix D for details. Table 4 (second column) shows that SoViT-400m/14 is competitive with ViT-g/14, and substantially better than ViT-L/16.

5.3 Multitask Decoding

We also evaluate the three pretrained ViT models in multitask decoding as described in Section 4.2, where we follow the setup studied in [7]. We fix the decoder architecture to two layers since it was found to perform well [7]. For evaluation, we report COCO CIDEr, OCR, VQAv2 and GQA accuracy and log-perplexity. Results are summarized in Table 4. SoViT-400M performs on par with ViT-g/14.

5.4 Panoptic Segmentation

Additionally, we evaluate SoViT-400m/14 on panoptic segmentation [39], which is a challenging dense scene understating task by closely following the setup in UViM [41]. At a high level, UViM panoptic segmentation model consists of a visual image encoder and a decoder which maps the image representation to an intermediate code. The code is later decoded to the panoptic segmentation mask using a fixed VQVAE [68] model, which was pretrained on panoptic masks [41]. In our experiments we initialize UViM's image encoder with ViT-L/16, SoViT-400m/14 and ViT-g/14.

Following [41], we train the UViM model using the COCO panoptic dataset (with 512×512 input resolution) and report the PQ metric. We achieve 43.5, 43.7 and 44.8 PQ points for ViT-L/16, SoViT-400m/14 and ViT-g/14 respectively. Our results indicate that dense segmentation tasks can be a limitation of the proposed optimal model shape, and a different model shape might be derived in this domain. We leave this investigation for future work.

Figure 7: Flexification of SoViT-400m/14 (abbr. So/14). See Section 5.5.

5.5 Flexifying SoViT-400M

Finally, since we do not include the patch size (sequence length) as part of the shape optimization, we verify that this is not a limitation by *flexifying* [6] SoViT-400m/14 on ILSVRC2012 for 300 epochs. The performance of the resulting FlexiSoViT-400m is shown in Fig 7 as green
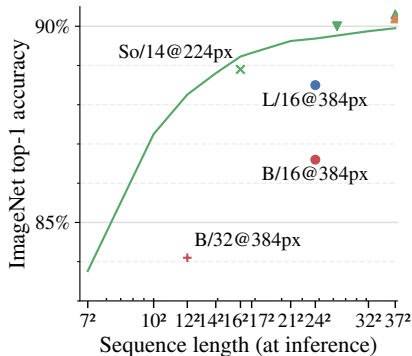
9

curve when varying the patch-size at inference time. A few reference ViT models from Table 1 and [76] are added, confirming that SoViT-400m maintains a clear advantage.

6 Conclusion

In conclusion, we introduce an efficient method for optimizing the shape of neural architectures and successfully apply it to vision transformers. Our analysis demonstrates that smaller models, trained at their optimal architecture shape for the right amount of compute, can match much larger models.

References

[1] Alabdulmohsin, I., Neyshabur, B., and Zhai, X. (2022). Revisiting neural scaling laws in language and vision. In *Advances in neural information processing systems (NeurIPS)*. 1, 4

[2] Bahri, Y., Dyer, E., Kaplan, J., Lee, J., and Sharma, U. (2021). Explaining neural scaling laws. *arXiv preprint arXiv:2102.06701*. 4, 6

[3] Bansal, Y., Ghorbani, B., Garg, A., Zhang, B., Krikun, M., Cherry, C., Neyshabur, B., and Firat, O. (2022). Data scaling laws in NMT: The effect of noise and architecture. *arXiv preprint arXiv:2202.01994*. 1, 4

[4] Bello, I., Fedus, W., Du, X., Cubuk, E. D., Srinivas, A., Lin, T.-Y., Shlens, J., and Zoph, B. (2021). Revisiting resnets: Improved training and scaling strategies. *Advances in neural information processing systems (NeurIPS)*. 2, 3, 5

[5] Beyer, L., Hénaff, O. J., Kolesnikov, A., Zhai, X., and van den Oord, A. (2020). Are we done with imagenet? *CoRR*, abs/2006.07159. 8, 19, 20

[6] Beyer, L., Izmailov, P., Kolesnikov, A., Caron, M., Kornblith, S., Zhai, X., Minderer, M., Tschannen, M., Alabdulmohsin, I., and Pavetic, F. (2023a). Flexivit: One model for all patch sizes. In *CVPR*. 6, 9

[7] Beyer, L., Wan, B., Madan, G., Pavetic, F., Steiner, A., Kolesnikov, A., Pinto, A. S., Bugliarello, E., Wang, X., Yu, Q., Chen, L.-C., and Zhai, X. (2023b). A study of autoregressive decoders for multi-tasking in computer vision. 6, 7, 9, 17

[8] Beyer, L., Zhai, X., and Kolesnikov, A. (2022a). Better plain vit baselines for imagenet-1k. 10

[9] Beyer, L., Zhai, X., and Kolesnikov, A. (2022b). Big vision. https://github.com/google-research/big_vision. 10

[10] Boyd, S. P. and Vandenberghe, L. (2004). *Convex optimization*. Cambridge university press. 15

[11] Brown, J. R., Zhao, Y., Shumailov, I., and Mullins, R. D. (2022). Wide attention is the way forward for transformers. *arXiv preprint arXiv:2210.00640*. 2, 3

[12] Brown, T., Mann, B., Ryder, N., Subbiah, M., Kaplan, J. D., Dhariwal, P., Neelakantan, A., Shyam, P., Sastry, G., Askell, A., et al. (2020). Language models are few-shot learners. *Advances in neural information processing systems (NeurIPS)*. 1, 2

[13] Chen, X., Fang, H., Lin, T.-Y., Vedantam, R., Gupta, S., Dollár, P., and Zitnick, C. L. (2015). Microsoft coco captions: Data collection and evaluation server. *arXiv preprint arXiv:1504.00325*. 7, 9

[14] Chen, X., Wang, X., Changpinyo, S., Piergiovanni, A., Padlewski, P., Salz, D., Goodman, S., Grycner, A., Mustafa, B., Beyer, L., Kolesnikov, A., Puigcerver, J., Ding, N., Rong, K., Akbari, H., Mishra, G., Xue, L., Thapliyal, A., Bradbury, J., Kuo, W., Seyedhosseini, M., Jia, C., Ayan, B. K., Riquelme, C., Steiner, A., Angelova, A., Zhai, X., Houlsby, N., and Soricut, R. (2022). Pali: A jointly-scaled multilingual language-image model. 3, 9

[15] Chowdhery, A., Narang, S., Devlin, J., Bosma, M., Mishra, G., Roberts, A., Barham, P., Chung, H. W., Sutton, C., Gehrmann, S., et al. (2022). Palm: Scaling language modeling with pathways. *arXiv preprint arXiv:2204.02311*. 1

[16] Cimpoi, M., Maji, S., Kokkinos, I., Mohamed, S., and Vedaldi, A. (2014). Describing textures in the wild. In *Proceedings of the IEEE Conf. on Computer Vision and Pattern Recognition (CVPR)*. 9

[17] Code, P. W. (2023). Papers With Code: ImageNet Benchmark. https://paperswithcode.com/sota/image-classification-on-imagenet. [Online; accessed 16-May-2023]. 8

[18] Dai, Z., Liu, H., Le, Q. V., and Tan, M. (2021). Coatnet: Marrying convolution and attention for all data sizes. *Advances in neural information processing systems (NeurIPS)*. 1, 8

[19] Dehghani, M., Arnab, A., Beyer, L., Vaswani, A., and Tay, Y. (2022). The efficiency misnomer. In *ICLR*. 3

[20] Dehghani, M., Djolonga, J., Mustafa, B., Padlewski, P., Heek, J., Gilmer, J., Steiner, A., Caron, M., Geirhos, R., Alabdulmohsin, I., Jenatton, R., Beyer, L., Tschannen, M., Arnab, A., Wang, X., Riquelme, C., Minderer, M., Puigcerver, J., Evci, U., Kumar, M., van Steenkiste, S., Elsayed, G. F., Mahendran, A., Yu, F., Oliver, A., Huot, F., Bastings, J., Collier, M. P., Gritsenko, A., Birodkar, V., Vasconcelos, C., Tay, Y., Mensink, T., Kolesnikov, A., Pavetić, F., Tran, D., Kipf, T., Lučić, M., Zhai, X., Keysers, D., Harmsen, J., and Houlsby, N. (2023). Scaling vision transformers to 22 billion parameters. 3

[21] Deng, J., Dong, W., Socher, R., Li, L.-J., Li, K., and Fei-Fei, L. (2009). Imagenet: A large-scale hierarchical image database. In *Conference on Computer Vision and Pattern Recognition (CVPR)*. 2, 9

[22] Devlin, J., Chang, M.-W., Lee, K., and Toutanova, K. (2018). Bert: Pre-training of deep bidirectional transformers for language understanding. *arXiv preprint arXiv:1810.04805*. 1

[23] Dosovitskiy, A., Beyer, L., Kolesnikov, A., Weissenborn, D., Zhai, X., Unterthiner, T., Dehghani, M., Minderer, M., Heigold, G., Gelly, S., et al. (2020). An image is worth 16x16 words: Transformers for image recognition at scale. *International Conference on Representation Learning (ICLR)*. 1, 2, 6, 7, 8

[24] Fei-Fei, L., Fergus, R., and Perona, P. (2004). Learning generative visual models from few training examples: An incremental bayesian approach tested on 101 object categories. *Conference on Computer Vision and Pattern Recognition (CVPR) Workshops*. 9

[25] Ghorbani, B., Firat, O., Freitag, M., Bapna, A., Krikun, M., Garcia, X., Chelba, C., and Cherry, C. (2021). Scaling laws for neural machine translation. *arXiv preprint arXiv:2109.07740*. 1

[26] Gordon, M. A., Duh, K., and Kaplan, J. (2021). Data and parameter scaling laws for neural machine translation. In *Conference on Empirical Methods in Natural Language Processing*. 1, 4

[27] Goyal, Y., Khot, T., Summers-Stay, D., Batra, D., and Parikh, D. (2017). Making the v in vqa matter: Elevating the role of image understanding in visual question answering. In *CVPR*. 7, 9

[28] He, K., Zhang, X., Ren, S., and Sun, J. (2016). Deep residual learning for image recognition. In *Conference on Computer Vision and Pattern Recognition (CVPR)*. 2

[29] Henighan, T., Kaplan, J., Katz, M., Chen, M., Hesse, C., Jackson, J., Jun, H., Brown, T. B., Dhariwal, P., Gray, S., et al. (2020). Scaling laws for autoregressive generative modeling. *arXiv preprint arXiv:2010.14701*. 1

[30] Hernandez, D., Kaplan, J., Henighan, T., and McCandlish, S. (2021). Scaling laws for transfer. *arXiv preprint arXiv:2102.01293*. 1

[31] Hestness, J., Narang, S., Ardalani, N., Diamos, G., Jun, H., Kianinejad, H., Patwary, M., Ali, M., Yang, Y., and Zhou, Y. (2017). Deep learning scaling is predictable, empirically. *arXiv preprint arXiv:1712.00409*. 1, 4

[32] Hoffmann, J., Borgeaud, S., Mensch, A., Buchatskaya, E., Cai, T., Rutherford, E., Casas, D. d. L., Hendricks, L. A., Welbl, J., Clark, A., et al. (2022). Training compute-optimal large language models. In *Advances in neural information processing systems (NeurIPS)*. 1, 2, 3, 4, 5

[33] Howard, A. G., Zhu, M., Chen, B., Kalenichenko, D., Wang, W., Weyand, T., Andreetto, M., and Adam, H. (2017). MobileNets: Efficient convolutional neural networks for mobile vision applications. *arXiv preprint arXiv:1704.04861*. 2, 3

[34] Hudson, D. A. and Manning, C. D. (2019). GQA: a new dataset for compositional question answering over real-world images. *arXiv preprint arXiv:1902.09506*. 7, 9

[35] Hutter, M. (2021). Learning curve theory. *arXiv preprint arXiv:2102.04074*. 4, 6

[36] Kaplan, J., McCandlish, S., Henighan, T., Brown, T. B., Chess, B., Child, R., Gray, S., Radford, A., Wu, J., and Amodei, D. (2020). Scaling laws for neural language models. *arXiv preprint arXiv:2001.08361*. 1, 3, 4, 5

[37] Kather, J. N., Weis, C.-A., Bianconi, F., Melchers, S. M., Schad, L. R., Gaiser, T., Marx, A., and Z"ollner, F. G. (2016). Multi-class texture analysis in colorectal cancer histology. *Scientific reports*, 6:27988. 9

[38] Kingma, D. P. and Ba, J. (2014). Adam: A method for stochastic optimization. *arXiv preprint arXiv:1412.6980*. 6

[39] Kirillov, A., He, K., Girshick, R., Rother, C., and Dollar, P. (2019). Panoptic segmentation. In *Conference on Computer Vision and Pattern Recognition (CVPR)*. 9

[40] Kolesnikov, A., Beyer, L., Zhai, X., Puigcerver, J., Yung, J., Gelly, S., and Houlsby, N. (2020). Big transfer (BiT): General visual representation learning. In *European Conference on Computer Vision (ECCV)*. 1, 2, 6, 8

[41] Kolesnikov, A., Susano Pinto, A., Beyer, L., Zhai, X., Harmsen, J., and Houlsby, N. (2022). UViM: A unified modeling approach for vision with learned guiding codes. *Advances in neural information processing systems (NeurIPS)*. 9

[42] Krause, J., Stark, M., Deng, J., and Fei-Fei, L. (2013). 3d object representations for fine-grained categorization. In *4th International IEEE Workshop on 3D Representation and Recognition (3dRR-13)*, Sydney, Australia. 9

[43] Krizhevsky, A. (2009). Learning multiple layers of features from tiny images. Technical report. 9

[44] Li, Z., Wallace, E., Shen, S., Lin, K., Keutzer, K., Klein, D., and Gonzalez, J. (2020). Train big, then compress: Rethinking model size for efficient training and inference of transformers. In *International Conference on Machine Learning (ICML)*. 1, 3

[45] Lin, T.-Y., Maire, M., Belongie, S., Hays, J., Perona, P., Ramanan, D., Dollár, P., and Zitnick, C. L. (2014). Microsoft coco: Common objects in context. In *ECCV*. 7

[46] Liu, Z., Hu, H., Lin, Y., Yao, Z., Xie, Z., Wei, Y., Ning, J., Cao, Y., Zhang, Z., Dong, L., et al. (2022). Swin transformer v2: Scaling up capacity and resolution. In *Proceedings of the IEEE/CVF conference on computer vision and pattern recognition*, pages 12009–12019. 3, 8

[47] Mishra, A., Shekhar, S., Singh, A. K., and Chakraborty, A. (2019). OCR-VQA: Visual question answering by reading text in images. In *ICDAR*. 7, 9

[48] Parkhi, O. M., Vedaldi, A., Zisserman, A., and Jawahar, C. V. (2012). Cats and dogs. In *IEEE Conference on Computer Vision and Pattern Recognition*. 9

[49] Patterson, D., Gonzalez, J., Le, Q., Liang, C., Munguia, L.-M., Rothchild, D., So, D., Texier, M., and Dean, J. (2021). Carbon emissions and large neural network training. *arXiv preprint arXiv:2104.10350*. 3

[50] Pham, H., Dai, Z., Ghiasi, G., Kawaguchi, K., Liu, H., Yu, A. W., Yu, J., Chen, Y.-T., Luong, M.-T., Wu, Y., et al. (2021). Combined scaling for zero-shot transfer learning. *arXiv preprint arXiv:2111.10050*. 18

[51] Radford, A., Kim, J. W., Hallacy, C., Ramesh, A., Goh, G., Agarwal, S., Sastry, G., Askell, A., Mishkin, P., Clark, J., et al. (2021). Learning transferable visual models from natural language supervision. In *ICML*. 9

[52] Rae, J. W., Borgeaud, S., Cai, T., Millican, K., Hoffmann, J., Song, F., Aslanides, J., Henderson, S., Ring, R., Young, S., et al. (2021). Scaling language models: Methods, analysis & insights from training gopher. *arXiv preprint arXiv:2112.11446*. 1, 2, 3

[53] Recht, B., Roelofs, R., Schmidt, L., and Shankar, V. (2019). Do imagenet classifiers generalize to imagenet? *CoRR*, abs/1902.10811. 8

[54] Russakovsky, O., Deng, J., Su, H., Krause, J., Satheesh, S., Ma, S., Huang, Z., Karpathy, A., Khosla, A., Bernstein, M. S., Berg, A. C., and Fei-Fei, L. (2014). Imagenet large scale visual recognition challenge. *CoRR*, abs/1409.0575. 8

[55] Sandler, M., Howard, A., Zhu, M., Zhmoginov, A., and Chen, L.-C. (2018). MobileNetV2: Inverted residuals and linear bottlenecks. In *Conference on Computer Vision and Pattern Recognition (CVPR)*. 2

[56] Sharma, U. and Kaplan, J. (2022). Scaling laws from the data manifold dimension. *Journal of Machine Learning Research*, 23. 4, 6

[57] Shazeer, N. and Stern, M. (2018). Adafactor: Adaptive learning rates with sublinear memory cost. In *International Conference on Machine Learning (ICML)*. 16, 17, 18

[58] Singh, M., Duval, Q., Alwala, K. V., Fan, H., Aggarwal, V., Adcock, A., Joulin, A., Dollár, P., Feichtenhofer, C., Girshick, R., et al. (2023). The effectiveness of mae pre-pretraining for billion-scale pretraining. *arXiv preprint arXiv:2303.13496*. 3, 8

[59] Steiner, A. P., Kolesnikov, A., Zhai, X., Wightman, R., Uszkoreit, J., and Beyer, L. (2022). How to train your vit? data, augmentation, and regularization in vision transformers. *Transactions on Machine Learning Research*. 3

[60] Sun, C., Shrivastava, A., Singh, S., and Gupta, A. (2017). Revisiting unreasonable effectiveness of data in deep learning era. In *International Conference on Computer Vision (ICCV)*. 2

[61] Tan, M. and Le, Q. (2019). EfficientNet: Rethinking model scaling for convolutional neural networks. In *International Conference on Machine Learning (ICML)*. 1, 2, 3

[62] Tay, Y., Dehghani, M., Abnar, S., Chung, H. W., Fedus, W., Rao, J., Narang, S., Tran, V. Q., Yogatama, D., and Metzler, D. (2022a). Scaling laws vs model architectures: How does inductive bias influence scaling? *arXiv preprint arXiv:2207.10551*. 3

[63] Tay, Y., Dehghani, M., Rao, J., Fedus, W., Abnar, S., Chung, H. W., Narang, S., Yogatama, D., Vaswani, A., and Metzler, D. (2022b). Scale efficiently: Insights from pre-training and fine-tuning transformers. In *International Conference on Representation Learning (ICLR)*. 2, 3

[64] Touvron, H., Cord, M., Douze, M., Massa, F., Sablayrolles, A., and Jégou, H. (2021). Training data-efficient image transformers & distillation through attention. In *International Conference on Machine Learning (ICML)*. 3

[65] Touvron, H., Cord, M., and Jégou, H. (2022). DeiT III: Revenge of the ViT. In *Computer Vision– ECCV 2022: 17th European Conference, Tel Aviv, Israel, October 23–27, 2022, Proceedings, Part XXIV*, pages 516–533. Springer. 3

[66] Touvron, H., Lavril, T., Izacard, G., Martinet, X., Lachaux, M.-A., Lacroix, T., Rozière, B., Goyal, N., Hambro, E., Azhar, F., Rodriguez, A., Joulin, A., Grave, E., and Lample, G. (2023). Llama: Open and efficient foundation language models. 2, 3

[67] Touvron, H., Vedaldi, A., Douze, M., and Jégou, H. (2019). Fixing the train-test resolution discrepancy. *Advances in neural information processing systems*, 32. 8

[68] Van Den Oord, A., Vinyals, O., et al. (2017). Neural discrete representation learning. *Advances in neural information processing systems (NeurIPS)*. 9

[69] Vaswani, A., Shazeer, N., Parmar, N., Uszkoreit, J., Jones, L., Gomez, A. N., Kaiser, Ł., and Polosukhin, I. (2017). Attention is all you need. *Advances in neural information processing systems (NeurIPS)*. 7

[70] Welinder, P., Branson, S., Mita, T., Wah, C., Schroff, F., Belongie, S., and Perona, P. (2010). Caltech-UCSD Birds 200. Technical Report CNS-TR-2010-001, California Institute of Technology. 9

[71] Wu, Z., Shen, C., and Van Den Hengel, A. (2019). Wider or deeper: Revisiting the resnet model for visual recognition. *Pattern Recognition*. 2

[72] Yang, Y. and Newsam, S. (2010). Bag-of-visual-words and spatial extensions for land-use classification. In *ACM SIGSPATIAL International Conference on Advances in Geographic Information Systems (ACM GIS)*. 9

[73] Yu, J., Wang, Z., Vasudevan, V., Yeung, L., Seyedhosseini, M., and Wu, Y. (2022). CoCa: Contrastive captioners are image-text foundation models. *arXiv preprint arXiv:2205.01917*. 8

[74] Yuan, L., Chen, D., Chen, Y.-L., Codella, N., Dai, X., Gao, J., Hu, H., Huang, X., Li, B., Li, C., et al. (2021). Florence: A new foundation model for computer vision. *arXiv preprint arXiv:2111.11432*. 3

[75] Zagoruyko, S. and Komodakis, N. (2016). Wide residual networks. *arXiv preprint arXiv:1605.07146*. 2

[76] Zhai, X., Kolesnikov, A., Houlsby, N., and Beyer, L. (2022a). Scaling vision transformers. In *Conference on Computer Vision and Pattern Recognition (CVPR)*. 1, 2, 3, 4, 6, 8, 10

[77] Zhai, X., Wang, X., Mustafa, B., Steiner, A., Keysers, D., Kolesnikov, A., and Beyer, L. (2022b). LiT: Zero-shot transfer with locked-image text tuning. In *CVPR*, pages 18123–18133. 2, 9

A Scaling Laws Analysis

In this appendix, we present proofs of two claims in the paper. First, we show that (2) is quasiconvex on its first argument $\mathbf{x}_k$. Second, we derive (5).

A.1 Quasiconvexity Proof

We assume throughout the proof that a_k, b_k are strictly positive, otherwise $f_k(\mathbf{x}_k, \mathbf{t})$ is a monotone function on its first argument and the statement holds trivially.

To establish the quasiconvexity of $f_k(\mathbf{x}_k, \mathbf{t})$ in (2), we observe that:

$$\frac{\partial f_k}{\partial \mathbf{x}_k} = -\alpha_k a_k \mathbf{x}_k^{-(1+a_k)} + \beta_k b_k \mathbf{t}^{-c} \mathbf{x}^{b_k - 1} \doteq -A \mathbf{x}_k^{-(1+a_k)} + B \mathbf{x}^{b_k - 1}.$$

Setting the derivative to zero gives the *unique* solution in $\mathbb{R}^+$:

$$\hat{\mathbf{x}} = \left(\frac{A}{B} \right)^{\frac{1}{a_k + b_k}}.$$

At the limit $\mathbf{x}_k \to \infty$, the term involving $\mathbf{x}_k^{-a_k}$ vanishes and we have the asymptotic relation:

$$f_k(\mathbf{x}_k, \mathbf{t}) \sim \beta_k \mathbf{t}^{-c} \mathbf{x}^{b_k},$$

which is an increasing function since $b_k > 0$. Since $\hat{x}$ is the only point in $\mathbb{R}^+$ where $\partial f_k / \partial \mathbf{x}_k = 0$, we conclude that $f(\mathbf{x}_k, \mathbf{t})$ is monotone increasing for all $\mathbf{x}_k \geq \hat{x}$.

Similarly, when $\mathbf{x}_k \to 0^+$, we have:

$$f_k(\mathbf{x}_k, \mathbf{t}) \sim \alpha_k \mathbf{x}_k^{-a_k},$$

which is monotone decreasing. Therefore, $f'(\mathbf{x}_k, \mathbf{t}) \leq 0$ for all $\mathbf{x}_k \leq \hat{x}$. Combining both results implies that $f_k(x, \mathbf{t})$ is monotone decreasing in the domain $x \in (0, \hat{x})$ and is monotone increasing in the domain $x \in (\hat{x}, \infty)$.

A function $f(y)$ is said to be quasi-convex if for any y_1 and y_2 in its domain and any $\lambda \in [0, 1]$, one has [10]:

$$f(\lambda y_1 + (1 - \lambda) y_2) \leq \max \{ f(y_1), f(y_2) \}. \tag{6}$$

Suppose for the purpose of obtaining a contradiction that $f_k(\mathbf{x}_k, \mathbf{t})$ is not quasiconvex on its first argument. Then, there exists two points $y_1, y_2 \in \mathbb{R}^+$ and $\lambda \in [0, 1]$ such that the above condition is violated. Let $\hat{y} = \lambda y_1 + (1 - \lambda) y_2$. But, then, by the mean-value theorem, there must exist two points $c_1 \in [y_1, \hat{y}]$ and $c_2 \in [\hat{y}, y_2]$ where:

$$f_k'(c_1) = \frac{f(\hat{y}) - f(y_1)}{\hat{y} - y_1} \geq 0$$

$$f_k'(c_2) = \frac{f(y_2) - f(\hat{y})}{y_2 - \hat{y}} \leq 0,$$

with $c_2 > c_1$. This implies that $c_1 \geq \hat{x}$ and $c_2 \leq \hat{x}$, which is a contradiction. Therefore, $f_k(\mathbf{x}_k, \mathbf{t})$ is quasi-convex on its first argument.

A.2 Derivation of (5)

Rearranging the expression in (4), we have:

$$\left(\frac{\beta_k b_k}{\alpha_k a_k} \right) (\mathbf{x}_k^\star)^{b_k + a_k} = \mathbf{t}^c$$

From this and (2), we obtain:

$$f_k(\mathbf{x}_k^\star, \mathbf{t}) = \alpha_k (\mathbf{x}_k^\star)^{-a_k} + \beta_k (\mathbf{x}_k^\star)^{b_k} \left(\frac{\alpha_k a_k}{\beta_k b_k (\mathbf{x}_k^\star)^{b_k + a_k}} \right) + \xi_k \mathbf{t}^{-c} + \varepsilon_k,$$

where we plugged in the last expression. Simplifying yields (5) for some constants $F, G \geq 0$.

15

B Shape Optimization

B.1 Hyper-parameters

Table 5: Common hyper-parameters settings for both star and grid sweeps.

Image Resolution	224×224
Batch size	128
Preprocessing	Rescale(-1, 1)
Augmentation	InceptionCrop, Left-Right Flip
Optimizer	AdaFactor [57]
Gradient Clipping	1.0
Learning Rate	8e-4
Label Smoothing	0
Weight Decay	$0.03 \times$ 8e-4
Schedule	Reverse SQRT, 10K Warmup steps, 50K Cooldown steps

Table 5 provides the set of hyperparameters used in the star and grid sweeps. We use a small batch size of 128 here in order to train multiple models in parallel on small hardware topologies.

B.2 Star Sweep

In the star sweep, we use the center $\mathbf{x}^{(c)} = (1968, 40, 6144)$ as our starting point. To estimate the scaling exponents s_k in (4) for each dimension separately, we vary `width` in the grid $(608, 768, 928, 1088, 1328, 1648)$, `depth` in the grid $(8, 10, 12, 16, 20, 24)$, and `MLP dim` in the grid $(1088, 1360, 1728, 2160, 2592, 3072)$. We train each model on 500K, 1M, and 2M steps. We always fix the patch size to 14×14 and the number of attention heads to 16.

B.3 Grid Sweep

In the grid sweep, we pretrain each architecture on 600M examples. We use the cross-product of:

1. `width`: 416, 512, 608, 768
2. `depth`: 6, 8, 10, 12
3. `MLP Size`: 768, 928, 1088, 1360

C Multitask Decoding Setup

Table 6: Multi-task decoding Hyperparameter Settings.

Image Resolution	224×224
Batch size	512
Preprocessing	Rescale(-1, 1), ResizeSmall(256), CentralCrop(224)
Augmentation	InceptionCrop(224), Left-Right Flip
Optimizer	AdaFactor [57]
Epochs	50
Gradient Clipping	1.0
Label Smoothing	0.1
Learning Rate	3e-4
Weight Decay	1e-4
Schedule	Cosine, 10% Warmup period
Vocabulary Size	32k
Encoder Dropout Rate	0
Decoder Dropout Rate	0.1

Table 6 summarizes the hyperparameter settings for the multitask decoding setup in Section 4.2 and Section 5.3. We always fix the decoder to 2 layers since it generally performs well [7].

D   LiT Training Setup

Table 7: Locked-image text tuning (LiT) Hyperparameter Settings.

Image Resolution	224×224
Batch size	32K
Preprocessing	Rescale(-1, 1)
Augmentation	None
Optimizer	AdaFactor [57]
Total Examples	900M
Gradient Clipping	1.0
Learning Rate	1e-3
Weight Decay	1e-4
Schedule	Cosine, 20% Warmup period
Vocabulary Size	32k
Bias Init	-10
Temperature Init	10
Internal Representation	1,152

Table 7 summarizes the hyperparameter settings for the locked-image text turning (LiT) setup, which is used to report zero-shot classification accuracy in Table 4. We use a large batch size of 32K in this setup because it improves the performance of contrastive training [50].

Table 8: ImageNet fine-tuning settings. Settings in the first section vary with resolution, settings in the middle section were explored, and settings in the last section are unexplored good defaults.

	Full model fine-tuning		
	224 px	384 px	518 px
Learning rate decay	0.85	0.9	0.9
Random augment	-	2,10	2,10
Mixup	-	0.2	0.2
Training duration	50 k steps (20 epochs)		
Learning rate	0.03		
Polyak averaging (EMA)	-		
Optimizer	SGD with 0.9 Momentum		
Gradient clipping	1.0		
Weight decay	-		
Batch size	512		
Learning rate schedule	Cosine with 500 steps linear warmup		
Image crop	`inception_crop` (RandomResize)		
Random flip	Horizontal		
Loss	Sigmoid cross-entropy [5]		
Head init	kernel=0, bias=-6.9		
Train and minival splits	`train[:98%]` and `train[98%:]`		

E   Transfer to ImageNet-1k

E.1   Full model fine-tuning

Table 8 lists the settings for the ImageNet-1k fine-tuning results presented in Table 1 in the main paper. The only three settings which differ across resolutions are learningrate decay, random augment and mixup strenghts. We did explore various learningrates, training durations (mostly shorter) as well as Polyak averaging, although the same setting shown in the table appears to be best across the board. Finally, we list various other settings which we did not explore. We simply used good default values from experience.

E.2   Linear probe on frozen encoder

We take the image representation at the pre-logits, i.e. the 1152-dimensional vector that comes out of the MAP-head and feeds right into the linear classification layer. For each of ViT-L/16, SoViT-400m/14 and ViT-g/14, we perform a grid-search over the following settings, and select the best-performing model on minival (2% of train) to be reported in Table 2: **Augmentation**: `resize(256)|random_crop(224)` vs. `inception_crop(224)`, **learning rate**: 0.001, 0.0003, 0.0001, **epochs**: 1, 3, 10, **weight decay**: 0.0001, None. It should be noted that we keep various other settings to "known good defaults" based on prior explorations with similar models (i.e. plain ViTs). Table 9 summarizes key settings.

Table 9: ImageNet linear probing settings. Settings in the first section were grid-searched for each model, settings in the last section are unexplored good defaults.

| | Linear probe at 224 px | | |
	ViT-L/16	SoViT-400m/14	ViT-g/14
Learning rate	0.001	0.0003	0.001
Weight decay	0.0001	-	-
Training duration		24.7 k steps (10 epochs)	
Image crop		`resize(256)|random_crop(224)`	
Random augment		-	
Mixup		0.1	
Learning rate decay		-	
Polyak averaging (EMA)		-	
Optimizer		SGD with 0.9 Momentum	
Gradient clipping		-	
Batch size		512	
Learning rate schedule		Cosine with 10% linear warmup	
Random flip		Horizontal	
Loss		Sigmoid cross-entropy [5]	
Head init		kernel=0, bias=-6.9	
Train and minival splits		`train[:99%]` and `train[99%:]`	